

Anomalous double-layer restructuring in water-in-salt electrolytes at graphitic interfaces governs capacitance

Hannah O. Wood,^{*,a,b} Fulu Zhou,^{a,b} Jan Dočkal,^c Martin Lísal,^{d,c} Filip Moučka,^c Sittipong Kaewmorakot,^{a,e} Robert A. W. Dryfe,^{a,e} and Paola Carbone^{*,a}

^a*Department of Chemistry, University of Manchester, Oxford Road, Manchester M13 9PL, United Kingdom*

^b*Department of Chemical Engineering, University of Manchester, Oxford Road, Manchester M13 9PL, United Kingdom*

^c*Department of Physics, Faculty of Science, Jan Evangelista Purkyně University in Štít nad Labem, Pasteurova 3544/1, 400 96 Štít nad Labem, Czech Republic*

^d*Research Group of Molecular and Mesoscopic Modelling, Institute of Chemical Process Fundamentals, Czech Academy of Sciences, Rozvojová 135/1, 165 02 Prague, Czech Republic*

^e*Henry Royce Institute, University of Manchester, Oxford Road, Manchester M13 9PL, United Kingdom*

* E-mail: hannah.wood-3@manchester.ac.uk; paola.carbone@manchester.ac.uk

Abstract

The structure and thickness of the electrical double layer (EDL) at carbon electrodes strongly influence electrochemical performance, yet remain poorly understood in super-concentrated aqueous electrolytes. Here we combine classical and quantum-mechanical molecular dynamics simulations to resolve the interfacial organisation of aqueous

LiCl from dilute to water-in-salt (WiS) (1–20 mol kg^{−1}) concentrations at graphitic electrodes, and compare with electrochemical differential-capacitance measurements from which the potential of zero charge (PZC) is obtained. We uncover a concentration-driven restructuring of the EDL: below 6 mol kg^{−1}, solvated Li⁺ dominates the outer Helmholtz plane (OHP), but at higher concentrations co-adsorption of Cl[−] through solvent-separated ion pairs enforces a near 1:1 Li:Cl ratio at the interface. This transition expands the effective EDL thickness, redistributes the interfacial potential drop, and drives a decrease in the PZC, matching the trend inferred from differential-capacitance measurements on electrolyte-graphite interfaces. Capacitance calculations reveal that while both EDL and quantum contributions vary strongly with concentration, their opposing trends make the total capacitance appear nearly constant for pristine few-layer graphite; for electrodes with smaller quantum capacitance, however, the concentration dependence of the EDL capacitance would be directly reflected in the total capacitance. Solvent-separated ion pairing is identified as the key driver of anomalous EDL behaviour in LiCl WiS electrolytes, establishing design considerations for tuning interfacial capacitance and stability in next-generation aqueous energy-storage systems.

Introduction

At the interface between a charged surface and a liquid electrolyte, ions redistribute and solvent molecules reorient, forming an electrical double layer (EDL) that screens the surface charge. The composition, thickness and structure of the ions in this interfacial layer govern a myriad of processes in environmental, biological, and electrochemical contexts.^{1–5} Early continuum models treated the EDL as a single rigid Helmholtz capacitor. This description was later refined into the Gouy-Chapman-Stern (GCS) model,⁶ which assumes that the surface charge is neutralised in two layers: a compact (Stern) layer–locally distinguished into the inner Helmholtz plane (IHP) and outer Helmholtz plane (OHP)–in immediate contact

with the surface where counter-ions are strongly adsorbed, and a second, more mobile, diffuse (Gouy-Chapman) layer whose ion density decays towards the bulk solution following the Poisson-Boltzmann (PB) equation. This theoretical framework assumes (i) laterally homogeneous surface charge, (ii) point-like, non-interacting ions, and (iii) a structureless dielectric continuum.

Even at moderate ionic strength, however, the PB assumptions fail: finite ion size, van der Waals, dipolar/solvophobic effects, and strong Coulomb correlations drive specific ion adsorption and complex liquid structuring beyond mean-field theory.^{7–13} Extensions that include steric exclusion, dielectric decrement, and ion-ion correlations improve predictions,^{9,14–16} but atomistic simulations remain the most direct route to EDL structure.^{17–20} By resolving ion distributions, solvent layering, and interfacial dynamics, molecular dynamics (MD) simulations provide mechanistic access to adsorption free energies, capacitance, and how concentration controls ion accumulation at electrodes.^{21–23}

MD simulations incorporating explicit surface polarisation have highlighted ion-specific adsorption and nanoscale clustering at graphitic electrodes. Quantum mechanical molecular dynamics (QMMD) simulations by Elliott *et al.* revealed that smaller alkali cations retain their hydration shells and adsorb in the OHP, while larger ions, such as K^+ , partially dehydrate and penetrate the IHP.⁷ Further, they ascribed the asymmetry observed in experimentally measured total specific capacitance to the EDL capacitance (C_{EDL}) contribution, noting that C_{EDL} is larger at negative potentials because cations have a greater tendency for specific adsorption on graphene. Di Pasquale *et al.*, using constant chemical potential QMMD, demonstrated overscreening and substantial ion clustering in concentrated aqueous alkali halide solutions, a phenomenon traditionally associated with ionic liquids rather than aqueous electrolytes.^{2,24,25} More recent QMMD simulations of the graphene/aqueous electrolyte interface show that charging induces an asymmetric restructuring of the interfacial hydrogen-bond network, with positive potentials markedly increasing water-water hydrogen bonding while negative potentials produce only modest changes.²⁶ Dočkal *et al.* showed that charging

graphene reorients interfacial water, but individual molecules largely conserve their total number of intermolecular interactions with species by compensatory rearrangements.²⁷ They further demonstrated that larger, weakly hydrated ions adsorb predictably at oppositely charged graphene surfaces, whereas smaller ions can display counterintuitive enrichment (e.g. Li^+ at positively charged interfaces), highlighting the coupled roles of hydration-shell restructuring and solvent-mediated correlations in EDL formation. Finney *et al.* found that neutral graphite acquires an effective charge through preferential Na^+ adsorption, leading to anion accumulation and, above ~ 0.6 M, dense cation-anion stacking.²⁸ Subsequent work demonstrated that negative surface charge amplifies ion clustering and asymmetrically perturbs water orientation.²⁹ These findings highlight how surface polarisation and ion clustering drive rich interfacial structuring not captured by classical continuum models. Super-concentrated, or “water-in-salt” (WiS), electrolytes push ionic strength to extremes in which solvent molecules become scarce, ion-pairing is enhanced, and conventional solvation shells collapse. These structural features yield wide electrochemical stability windows, suppressed water activity, and unusual transport properties, positioning WiS-based systems as promising electrolytes for high-voltage aqueous batteries and capacitors.^{30–32} Yet their interfacial structure at carbon electrodes—particularly in alkali-halide WiS electrolytes—and its influence on observables such as capacitance remain largely unexplored.

A central descriptor of interfacial structure is the EDL thickness (or effective screening length, λ_S). Classical Debye-Hückel theory predicts that the electrostatic potential decays exponentially over a length λ_D —the Debye length—and that the effective screening length $\lambda_S \approx \lambda_D$ falls monotonically as salt concentration increases. The GCS model, being grounded in the same PB (and thus Debye-Hückel) mean-field framework, likewise predicts an exponentially decaying potential and a screening length that falls with increasing ionic strength. Modern liquid-state theories that embed finite-ion size and correlations instead predict a minimum λ_S at the so-called Kirkwood line (the bulk concentration at which charge-charge correlations transition from monotonic to damped-oscillatory decay) followed by a modest increase at

higher concentrations.^{33–36} Force-measurement studies on concentrated electrolytes, however, report much larger values that grow approximately as λ_D^3 and extend tens of nanometres,³⁷ a phenomenon termed “underscreening”. Consequently, the value of the screening length in alkali-halide electrolytes with concentration remains an open and actively debated question. In the present work, we use classical MD and QMMD to simulate aqueous LiCl from moderate to WiS concentrations at neutral and charged graphitic electrodes. Novel scaled-charge force field models have facilitated the investigation of much higher concentration regimes than were previously accessible. From these simulations, we study the concentration-dependent EDL structure and determine both the EDL and quantum capacitances. Our simulations show a significant transition in the EDL structure and thickness on graphite, occurring above 4 mol kg⁻¹ for neutral surfaces and at even lower concentrations when charged. This transition is driven by the preferential adsorption of Li⁺ and substantial co-adsorption of Cl⁻ into the OHP via solvent-separated ion pairs. This co-adsorption in the OHP does not fully neutralise the electrode charge, leaving a residual field that drives alternating ion layers and expands the effective EDL thickness. Consequently, the potential of zero charge (PZC) decreases, the interfacial potential drop redistributes, and the C_{EDL} changes substantially, with direct consequences for electrochemical performance and electrolyte design. We validate the simulated concentration dependence of the PZC against values extracted from differential-capacitance measurements obtained via electrochemical impedance spectroscopy.

Methodology

Computational Model

We model a parallel-plate capacitor configuration, comprising a LiCl slab ($3 \times 3 \times 8 \text{ nm}^3$) confined between two graphite electrodes, each built from four stacked graphene sheets ($3 \times 3 \text{ nm}^2$); see Figure 1. A 6 nm vacuum gap along the surface normal was imposed to prevent interactions with periodic images.³⁸ We consider three surface-charge states, $\sigma^0 = 0$,

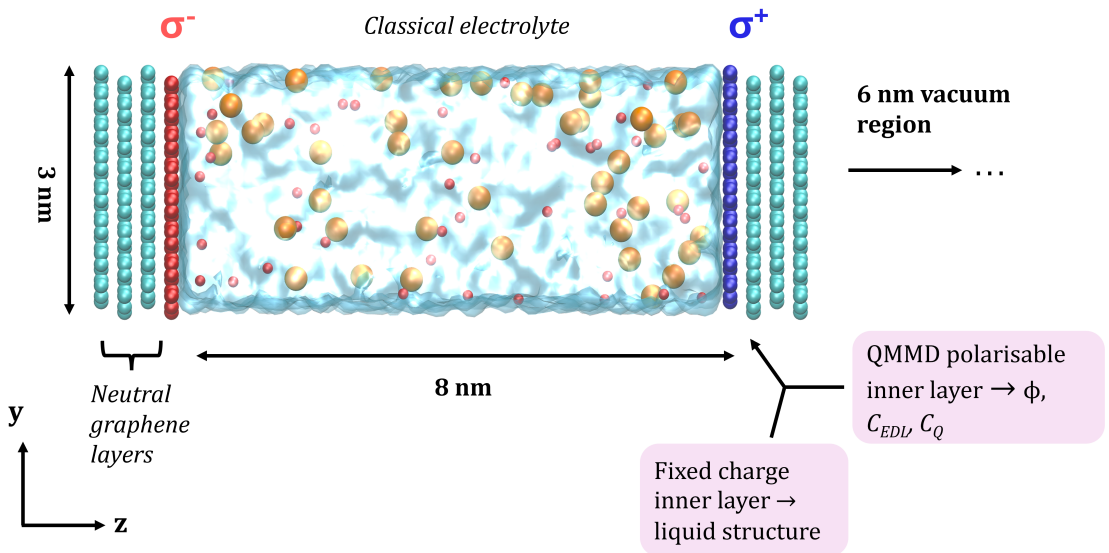


Figure 1: Schematic of the simulation cell showing a liquid electrolyte confined between two graphite electrodes in the x - y plane. Each electrode consists of four stacked graphene sheets; the innermost sheet carries a surface charge density of $\sigma^0 = 0 \text{ C m}^{-2}$ for neutral systems, or $\sigma^+ = +0.0571 \text{ C m}^{-2}$ (blue) and $\sigma^- = -0.0571 \text{ C m}^{-2}$ (red) in charged systems, while the three subsurface sheets remain neutral (cyan).

$\sigma^- = -0.0571$, and $\sigma^+ = +0.0571 \text{ C m}^{-2}$, applying charge only to the inner graphene layers in contact with the electrolyte. LiCl concentrations span $1\text{--}20 \text{ mol kg}^{-1}$ (1, 2, 4, 6, 10, 16, 20). Following Ref. 26, we use the Madrid-2019 ion force field,³⁹ TIP4P/2005 water constrained with SETTLE,⁴⁰ and take LJ parameters from Cornell *et al.*⁴¹ for the graphitic carbons. The C-O Lennard-Jones ε parameter is taken from Werder *et al.* to reproduce the experimental water/graphite contact angle,^{42,43} and ion-carbon non-bonded terms use Lorentz-Berthelot combining rules.

Classical MD

Classical MD simulations were performed with the GROMACS 2018.4 software package.^{44,45} Numbers of water molecules and ions were selected to reproduce the desired concentration and bulk density, as computed in our previous work,⁴⁶ with further details in the supporting information (SI). All simulations were carried out in the NVT ensemble with a Nosé-Hoover thermostat at 294.5 K (relaxation time 0.5 ps). The real-space cutoff for Lennard-Jones and Coulomb interactions was 1.2 nm. Long-range electrostatics were treated with particle-mesh Ewald (standard 3D geometry). The Lennard-Jones 12–6 potential used a switching function from 1.0 to 1.2 nm to smooth the truncation. Graphite electrode atoms are frozen in space during the simulation. Trajectories for $1\text{--}6 \text{ mol kg}^{-1}$ ran 450 ns, whereas those above 6 mol kg^{-1} were extended to 750 ns to obtain more statistically robust data. This extension is justified by our previous work, which showed that LiCl solutions with high concentrations require longer simulation times to reach thermodynamic equilibrium.⁴⁶

QMMD

For the calculation of total capacitance, we simulated the capacitor introduced in previous section with the QMMD scheme of Elliott *et al.*⁴⁷ In this iterative method, the electronic structure of the innermost graphite layer is updated by self-consistent-charge density-functional tight binding (SCC-DFTB) calculations, while the positions of the electrolyte atoms are

propagated by classical MD (with frozen electrode carbon atoms). At each quantum step, the SCC-DFTB Hamiltonian incorporates the instantaneous electrostatic field produced by the MD point charges; a Mulliken population analysis maps the resulting charge distribution onto partial charges of the carbon atoms, enabling the electrode to polarise self-consistently in response to its ionic environment. Quantum and classical subsystems are coupled every 5 ps: after each 5 ps segment of MD, a new SCC-DFTB step is performed to refresh the carbon charges, a coupling interval validated in previous works.⁴⁷

The MD parameters employed in QMMD calculations match those of the fully classical simulations described in classical MD section. Electronic-structure updates were performed with the DFTB+ software package,⁴⁸ with the `mio-1-1` parameter set for C-C interactions.⁴⁹ Calculations were restricted to the Γ -point with a Fermi smearing of 1×10^{-6} K. The self-consistent-charge cycle was considered converged when the total energy changed by less than 1×10^{-2} Ha. These settings have been shown to reproduce the surface charge distribution obtained from higher-level quantum-mechanical calculations within statistical uncertainty.^{7,47} Each system was first equilibrated for 60 ns under NVT conditions, followed by a 30 ns production run with the QMMD scheme.

Experimental methods

Capacitance measurements were conducted on the basal plane of highly oriented pyrolytic graphite (HOPG) using electrochemical impedance spectroscopy (EIS) over a frequency range of 20 kHz–1 Hz with a 7 mV rms amplitude. The electrochemical cell configuration used a polytetrafluoroethylene cylinder with a disk-shaped opening of 3 mm. A poly(dimethylsiloxane) gel layer (SylgardTM 527, Dow Corning) was used to seal between the bottom of the PTFE cylinder and the HOPG to prevent solution leakage. The application of potentials for EIS starts from 0 V (vs Ag/AgCl in 3.5 M KCl), with 50 mV potential steps, alternating between positive and negative potentials.

The effective capacitance (C_{eff}) at each frequency was then calculated from the EIS data by

adopting a method developed by Orazem and colleagues,⁵⁰

$$C_{\text{eff}} = -\sin\left(\frac{\alpha\pi}{2}\right) \frac{1}{Z_{\text{im}}(2\pi f)^\alpha}, \quad (1)$$

where Z_{im} is the imaginary part of the impedance and f is the frequency. The parameter α is the constant-phase-element exponent, which can be estimated from the slope between $\log f$ and $\log Z_{\text{im}}$. The final capacitance values were determined by averaging C_{eff} from the frequency range of 10 Hz to 100 Hz.

Results and Discussion

Electrode/Electrolyte Interface Structure

To investigate the interfacial liquid structure, we first calculated the bulk-normalised number density $\tilde{n}(z)$ of ionic and solvent species along the surface-normal (z) direction,

$$\tilde{n}(z) = \frac{\rho(z)}{\rho_{\text{bulk}}}, \quad (2)$$

where ρ_{bulk} represents the number density of each species in the bulk region.

The near-surface region contains two characteristic planes—the IHP and the OHP—beyond which the density profiles decay in the diffuse layer (DL) towards bulk-like behaviour. The IHP is defined as the plane passing through the centre of the first adsorbed layer of species (predominantly water) and is therefore located at the maximum of the first peak in the water-oxygen density profile. Analogously, the OHP is defined as the plane through the centres of the second layer of species (first layer of solvated ions) and is therefore taken as the position of the first Li^+ peak, since Li^+ adsorption is observed at all surface charges and concentrations and occurs predominantly in the OHP. It is well established that cations in alkali chloride electrolytes reside closer to neutral graphitic surfaces than chloride anions.^{7,18,28,51} This reflects a free-energy balance involving favourable cation-surface interactions (captured explicitly

as cation- π polarisation in models including surface polarisability, or effectively through the Lennard-Jones cross terms in simpler models), hydration free energies, and entropic packing constraints. Previous studies have reported that neglecting cation- π interactions can underestimate cation adsorption;⁷ however, in our systems, comparison of QMMD (including surface polarisation) with classical MD showed no such underestimation. This may be due to our use of the scaled-charge Madrid-2019 ion model, which has been shown to reproduce interfacial properties of alkali cations. Despite the absence of imposed surface charge density, this specific cation adsorption produces a nonzero PZC, which can be regarded as an effective surface charge that renders a structured EDL in much the same way as an explicitly charged electrode.

The positions of the IHP and OHP were determined for each system. Although the absolute positions of the IHP and OHP shift slightly with surface charge, they are essentially insensitive to concentration for each charge state. In all distance-resolved plots, we mark the IHP and OHP with pink and cyan dotted lines, respectively, and a representative snapshot highlighting these planes is included in Figure 2 (a). Figure 2 shows $\tilde{n}(z)$ profiles of LiCl electrolytes at 1 mol kg⁻¹, 10 mol kg⁻¹, and 20 mol kg⁻¹ under different surface charges. Density profiles for other concentrations are provided in the SI.

For all non-charged systems, we observe that water molecules form layers near the graphite surface. The first water layer is located at approximately 0.32 nm from the graphite at the IHP, while the second layer appears around 0.60 nm. This interfacial structuring is consistent with previous studies⁵² on the graphite-water interface using the TIP4P/2005 water model. In all neutral systems, the first peak of Li⁺ appears approximately 0.39 nm from the surface, followed by a second peak around 0.70 nm. For Cl⁻, the first and second peaks are located at approximately 0.39 nm and 0.64 nm, respectively.

At concentrations below 6 mol kg⁻¹, we observe the clear adsorption of Li⁺ in the OHP at neutral graphite, with Cl⁻ predominantly residing farther from the surface.^{7,26} As the concentration of LiCl reaches 10 mol kg⁻¹, significant changes are observed in the distribution

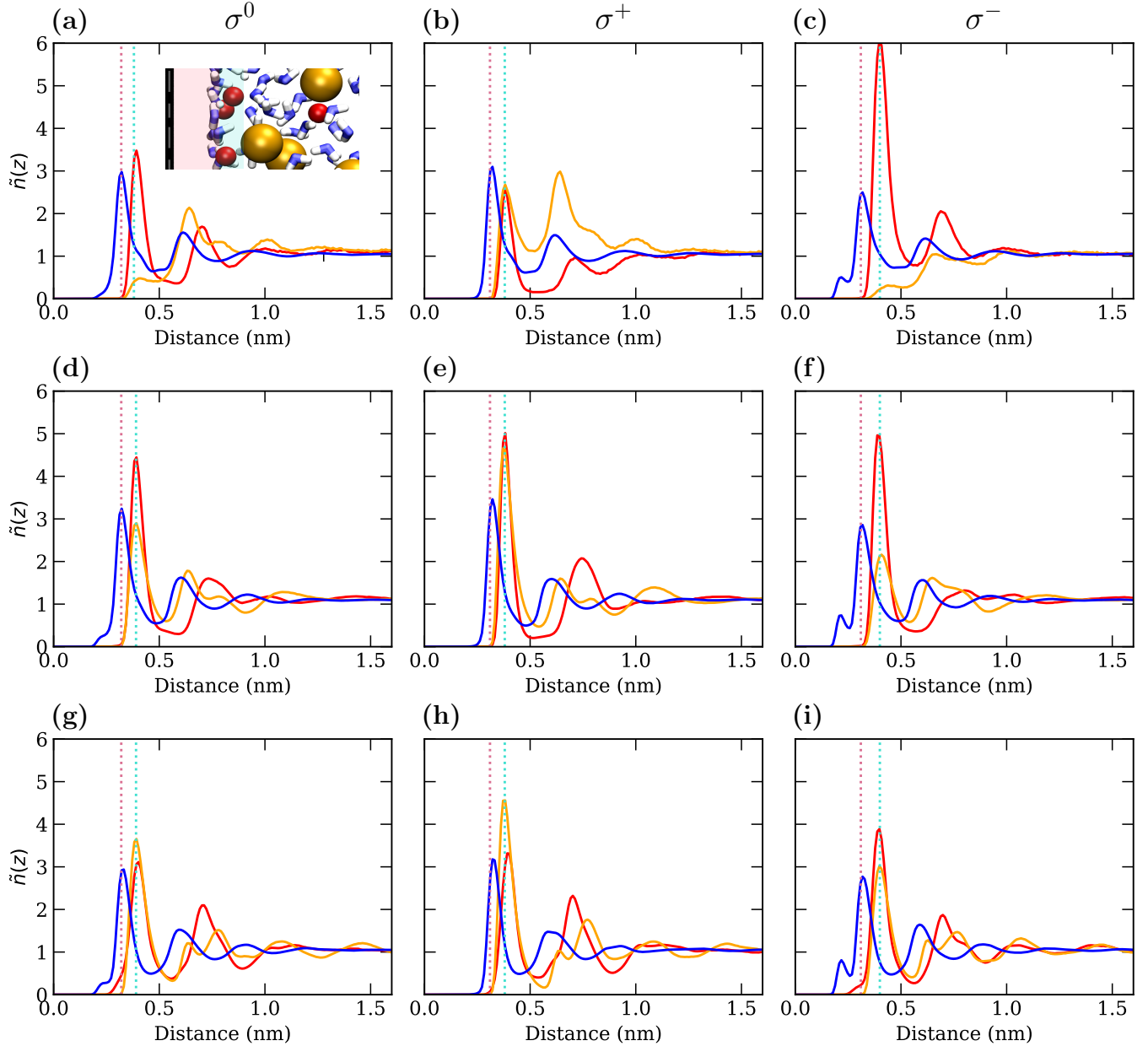


Figure 2: Bulk-normalised number-density profiles, $\tilde{n}(z)$, for Li^+ (red), Cl^- (orange), and water atoms (blue) as a function of distance z from the electrode surface. Columns correspond to electrode surface charge densities $\sigma^0 = 0 \text{ C m}^{-2}$ (left), $\sigma^+ = +0.0571 \text{ C m}^{-2}$ (middle), and $\sigma^- = -0.0571 \text{ C m}^{-2}$ (right). Rows show concentrations: (a–c) 1 mol kg^{-1} LiCl ; (d–f) 10 mol kg^{-1} ; (g–i) 20 mol kg^{-1} . Vertical dotted lines indicate the inner Helmholtz plane (IHP, pink) and outer Helmholtz plane (OHP, cyan).

of Cl^- ions: anions enter the OHP, accumulating at the same location as the Li^+ (shown in Figure 2 (d), where the Cl^- density profile first peak increases in height, surpassing that of its second peak). At 16 mol kg^{-1} , this accumulation of Cl^- becomes even more evident, and the peak intensity matches that of Li^+ (Figure S6 (a)). When the concentration reaches 20 mol kg^{-1} (Figure 2 (g)), the OHP Cl^- peak height exceeds that of Li^+ . At the same time, a small fraction of Li^+ extends into the IHP, as shown by the weak density tail beyond the pink dotted line, which lowers the proportion remaining in the OHP and decreases the Li^+ peak intensity.

The concentration-dependent redistribution of Cl^- ions becomes more pronounced once the electrode is charged. Figure S8 presents bulk-normalised density profiles of Li^+ and Cl^- across the full concentration range. At the positively charged electrode, Cl^- adsorption strengthens systematically: the accumulation shift evident in the neutral case already appears at 2 mol kg^{-1} , the first peak height becomes comparable to that of Li^+ by 10 mol kg^{-1} , and surpasses it at 16 mol kg^{-1} . On the negative electrode, Cl^- adsorption is weakened and shifted slightly outward relative to the neutral case, though appreciable density persists in the OHP at concentrations above 10 mol kg^{-1} , never exceeding that of Li^+ . In both polarities the water oxygen peaks retain their positions, although reorientation of the molecules occurs in response to the electrode charge.

Between 4 and 10 mol kg^{-1} , positive charging yields an enhanced Li^+ population in the OHP despite the expected electrostatic repulsion, with adsorption levels comparable to those at the negatively charged electrode and higher than at the neutral interface. At 20 mol kg^{-1} , positive charging suppresses the small Li^+ population in the IHP while leaving the OHP density essentially unchanged, whereas negative charging slightly increases the IHP density. Overall, Cl^- responds to electrode polarity in the expected manner-enhanced at positive, reduced at negative potentials—while Li^+ shows a weaker and in some cases counterintuitive response, particularly the OHP enhancement at the positively charged electrode in the $4 - 10 \text{ mol kg}^{-1}$ range (discussed further in the analysis of the local charge density).

Electric Double Layer Thickness

The thickness of the EDL at the electrode/electrolyte interface plays a critical role in determining electrochemical behaviour, and has been studied extensively in the literature.^{53–57} Traditionally, it is estimated using the Debye length, which assumes point-like ions and a dilute electrolyte under the PB framework and can be calculated from molecular simulations as the distance at which the cumulative ionic charge density $Q(z)$ reaches a plateau⁵⁴ or where the ionic profiles return to bulk-like values.⁵⁵

In this study, the thickness of the EDL is determined using a two-step approach: First, computing the accumulated charge density $Q(z)$ in the neutral system and the screening factor $S(z)$ in charged systems,

$$Q(z) = \int_0^z \rho_q^{\text{ion}}(z') \, dz' \quad (3)$$

$$S(z) = \frac{1}{\sigma} \int_0^z \rho_q^{\text{ion}}(z') \, dz' \quad (4)$$

Here, $\rho_q^{\text{ion}}(z')$ denotes the net ionic charge density as a function of the distance from the electrode, z , and σ is the surface charge of the electrode. As both $Q(z)$ and $S(z)$ show oscillatory behaviour, the resulting curves are fitted by an under-damped oscillation function,

$$f(z) = A(z) \cdot \cos(\omega z + \phi) + C \quad (5)$$

where $A(z)$ is an envelope function for the amplitude, ω is the angular frequency, ϕ is the phase change and C is the baseline offset. This approach has been applied previously to describe the decaying, oscillatory screening at electrified interfaces with concentrated electrolytes and ionic liquids.^{54,58} For concentrations ranging from 1 to 10 mol kg⁻¹, the accumulated charge profiles were fitted using a standard damped cosine model with a constant damping coefficient:

$$f(z) = A \cdot e^{-kz} \cdot \cos(\omega z + \phi) + C \quad (6)$$

where Ae^{-kz} represents the exponential decay envelope. However, at higher concentrations ($16 - 20 \text{ mol kg}^{-1}$), the oscillatory behaviour of $Q(z)$ (or $S(z)$) becomes significantly more pronounced, and the simple exponential damping fails to capture the persistence of oscillations. To address this, a variable damping model was employed, in which the damping coefficient decreases with distance,

$$f(z) = A \cdot e^{(-\frac{k_0}{1+z} \cdot z)} \cdot \cos(\omega z + \phi) + C. \quad (7)$$

Here, the damping rate $k(z) = \frac{k_0}{1+z}$ decreases with increasing z , allowing the fit to better account for the extended range and persistence of oscillations observed in high-concentration regimes. The EDL thickness is defined as the position $z = z^*$ where the deviation of the envelope function $\Delta A(z)$ falls below 5% of the maximum of the accumulated charge or screening factor, i.e.,

$$\Delta A(z^*) \leq 0.05 \cdot \max \{Q(z), S(z)\}. \quad (8)$$

Figure 3 (a) and (b) show representative snapshots of the electrolyte structure at the neutral graphite interface under concentrations of 1 mol kg^{-1} and 20 mol kg^{-1} , respectively. The corresponding accumulated charge density profiles $Q(z)$ are presented in Figure 3 (c) and (d), together with the fitted damped oscillatory curves. The results of the estimated thickness of EDL are summarized in Figure 3 (e) as a function of electrolyte concentration under three surface charge conditions. Further details on the thicknesses of individual layers are provided in the SI.

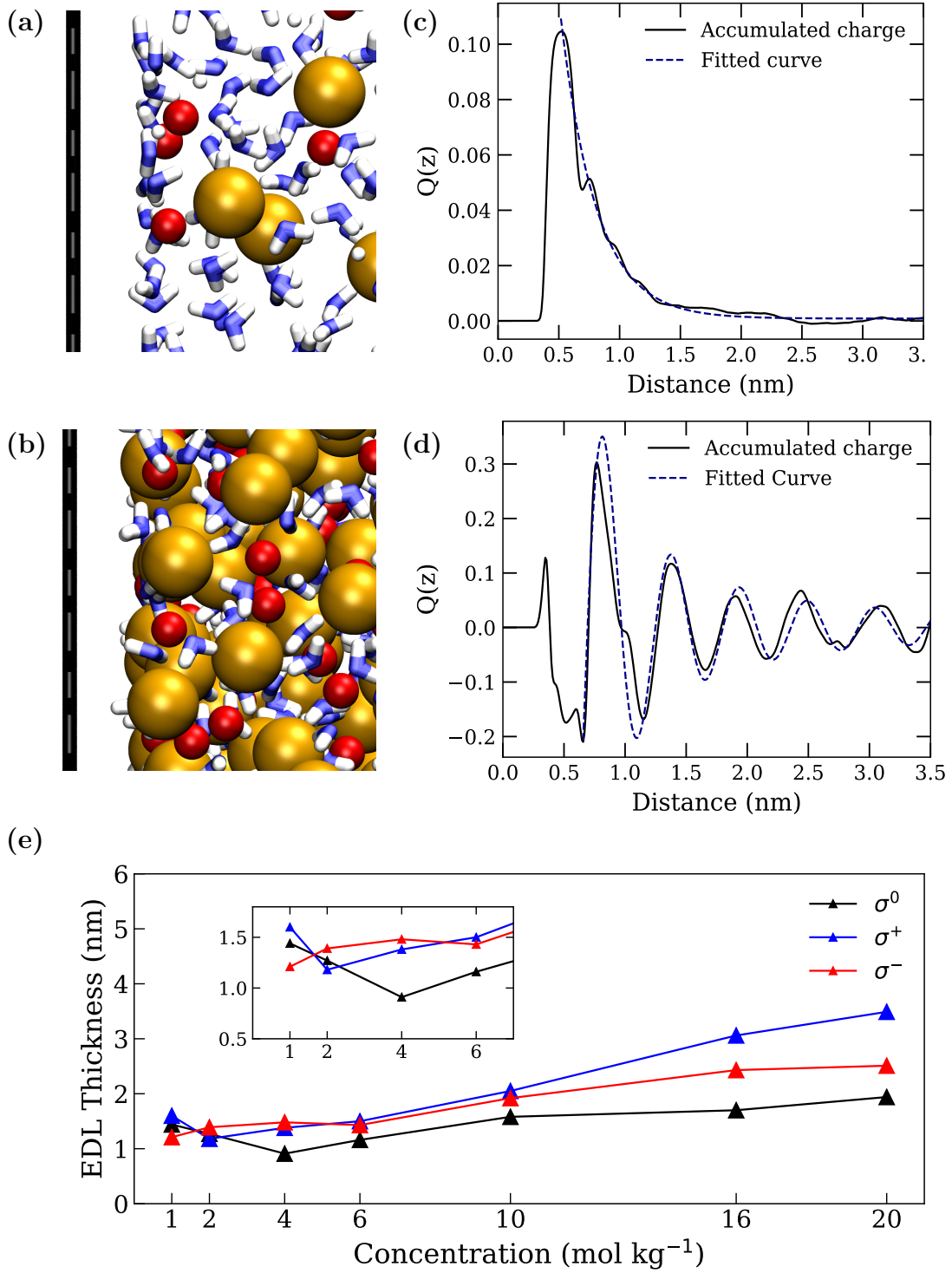


Figure 3: Electric double layer thickness estimation. (a, b) Snapshots of the interfacial region for 1 mol kg^{-1} and 20 mol kg^{-1} LiCl in contact with neutral graphite. (c, d) Accumulated charge density profiles $Q(z)$ (black solid line) near the neutral surface, together with fitted damped oscillatory curves (blue dashed line), corresponding to 1 mol kg^{-1} and 20 mol kg^{-1} LiCl. (e) EDL thickness as a function of electrolyte concentration under three surface charge conditions: σ^0 (black), σ^+ (blue), and σ^- (red).

In Debye-Hückel theory, EDL thickness decreases monotonically with concentration as additional ions are available to screen the surface charge; our data show a more complex trend. For the neutral case, the EDL thickness first decreases and then increases as the concentration of LiCl rises. We attribute this trend reversal to the enhanced oscillatory behaviour of ions at high concentrations. Although the thickness of the IHP and OHP remains relatively unchanged, the diffuse layer is significantly extended due to intensified ionic layering, thereby increasing the overall EDL thickness.

Under positively charged conditions, a similar non-monotonic trend is observed, with EDL thickness decreasing from $1 - 2 \text{ mol kg}^{-1}$, but increasing beyond 2 mol kg^{-1} : the onset of increasing thickness occurs at a lower ionic concentration compared with the neutral case. This is consistent with the earlier accumulation of Cl^- in the OHP, which induces overscreening and extends the oscillatory tail of $S(z)$, increasing the fitted EDL thickness. In contrast, for negatively charged surfaces, the EDL thickness increases monotonically with concentration. Below 6 mol kg^{-1} the EDL thickness changes only marginally. Although more Li^+ ions adsorb at the electrode at higher concentrations, the negative surface potential repels Cl^- out of the OHP. This reduces their capacity to counterbalance the excess Li^+ accumulation. Once the concentration exceeds 10 mol kg^{-1} , a clear accumulation shift of Cl^- ions is observed, resulting in an expansion of the diffuse layer.

Driving forces leading to the interfacial structural change

To understand the driving forces governing the concentration-induced restructuring of the EDL, we analyse the ions' local chemical environment using the procedure introduced by Dočkal and coworkers,⁵⁹ which uses topological features of the spatial distribution function to quantify properties such as hydration numbers and ion pairing. As the method does not rely on pre-defined distance-angle cut-offs, it enables transferable, non-redundant quantification of the local molecular arrangement, which is particularly important in the context of WiS electrolytes, where liquid structure deviates substantially from the dilute regimes for which conventional

cut-off-based criteria were developed. The method works by defining "intermolecular bonds" using the spatial distribution function (SDF), which gives the relative probability of finding a monitored particle (in our case O, H, Li^+ , or Cl^-) at a position (x, y, z) relative to a reference (water) molecule. Regions of high probability in the SDF (local maxima) indicate favoured positions around the monitored species. An intermolecular bond is considered to exist when the particle is located within a continuous volumetric region surrounding such a maximum; this volume is bounded by the isosurface that intersects the nearest "significant" saddle point (NSSP).⁵⁹ This approach ensures that only particles in well-defined, high-probability regions, corresponding to physically meaningful interactions, are counted as bonded. Using these bonding criteria, we determine both the ion-water hydration number, N_{hyd} , and the number of solvent-separated ion pairs (SSIPs), N_{SSIP} , which we identify as pairs of oppositely charged ions that are bonded to a common water molecule. The z -resolved results for neutral graphite systems are presented in Figure 4 (a, b). Across all z and for both σ^+ and σ^- electrodes, no contact ion pairs were detected for LiCl concentrations $\leq 10 \text{ mol kg}^{-1}$;⁶⁰ at 16 and 20 mol kg^{-1} only a minor contact ion pair population appears, with mean Li coordination numbers (over all z) of $N_{\text{Li-H}_2\text{O}} = 3.9$ and $N_{\text{Li-Cl}} = 0.1$ at 16 mol kg^{-1} , and 3.5 and 0.5 at 20 mol kg^{-1} , respectively. The hydration number of Li^+ is essentially concentration-independent: it remains $N_{\text{hyd}} \simeq 4$ at 1 and 10 mol kg^{-1} and decreases only slightly to ~ 3.5 at 20 mol kg^{-1} . This small drop reflects the scarcity of free water in the WiS regime. Throughout the bulk liquid, diffuse layer, and OHP, the Li^+ hydration number N_{hyd} is essentially independent of z . Figure 2 reveals that a small fraction of Li^+ ions penetrate into the IHP—most conspicuously at 20 mol kg^{-1} —as evidenced by the tail of the first cation density peak into this region. Once inside the IHP, N_{hyd} decreases to ~ 3 , while the Li^+ in the OHP retain their full primary hydration shell.⁷ Chloride behaves differently: the anions never enter the IHP, and their hydration number drops from ~ 5.8 at 1 and 10 mol kg^{-1} , reflecting a mixture of typical penta-/hexa-coordinated configurations, to ~ 4.8 at 20 mol kg^{-1} . Because Cl^- is larger and more weakly hydrated, it loses water molecules more readily in the WiS

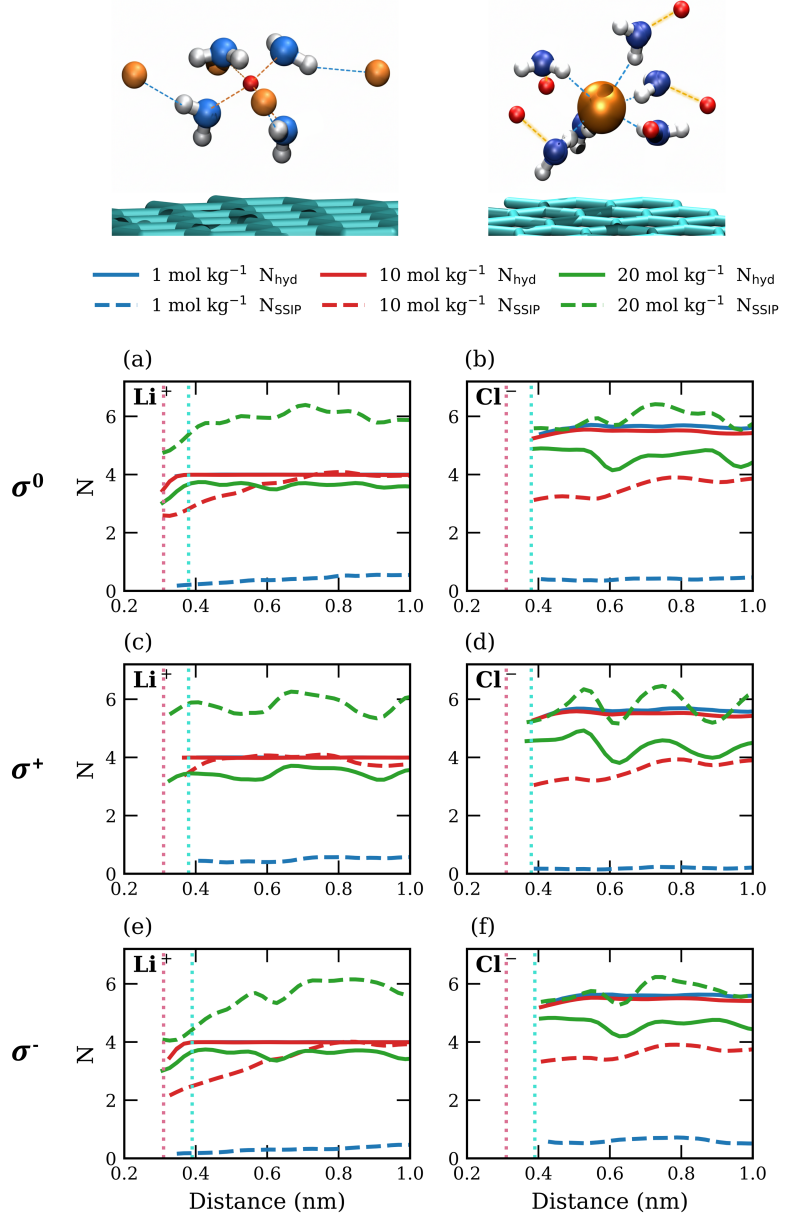


Figure 4: Hydration number, N_{hyd} , calculated as the mean number of H_2O -ion intermolecular bonds per ion (solid lines), and solvent-separated ion pairs per ion, N_{SSIP} (dashed lines), as a function of distance from the electrode for Li^+ (left column) and Cl^- (right column). Concentrations of 1, 10, and 20 mol kg^{-1} are shown in blue, red, and green, respectively. Vertical dotted lines mark the inner Helmholtz plane (IHP, pink) and the outer Helmholtz plane (OHP, cyan). Row labels indicate the electrode surface charge: σ^0 (top row, neutral), $\sigma^+ = +0.0571 \text{ C m}^{-2}$ (middle row), and $\sigma^- = -0.0571 \text{ C m}^{-2}$ (bottom row). The images above depict representative hydration motifs for Li^+ (left) and Cl^- (right).

environment.

The number of SSIPs rises sharply with concentration, from ≈ 0.5 per Li^+ at 1 mol kg^{-1} to ~ 3.8 at 10 mol kg^{-1} and ~ 5.8 at 20 mol kg^{-1} . SSIPs are slightly less abundant in the OHP and IHP than in the diffuse and bulk regions, decreasing to approximately 3.0 per Li at 10 mol kg^{-1} and 5.4 per Li at 20 mol kg^{-1} . A modest suppression of SSIPs in the first ion adsorption layer is unsurprising, where a rigid surface creates geometric restriction.

These results indicate that the equal densities of Li^+ and Cl^- in the OHP of the WiS solutions arise because Li^+ retains a tightly bound first hydration shell, even at high concentrations. Each Li^+ remains coordinated to ~ 4 water molecules across all salt concentrations, thanks to its small radius and strongly negative hydration free energy.⁶¹ Therefore, Li^+ -bound water molecules are left with two H-donor sites that must be satisfied; in dilute solutions, they hydrogen-bond to other waters, but in the WiS regime, there are too few free waters available. Instead, those donors attach to nearby Cl^- , creating solvent-separated $\text{Li}^+ - \text{Cl}^-$ pairs. Thus every Li^+ adsorbed at the graphite interface drags in accompanying Cl^- anions through its hydration shell, driving the interfacial Li:Cl ratio toward 1:1. In more dilute electrolytes the excess solvent completes the hydrogen-bond network with additional water molecules and Li^+ adsorption remains dominant.

Figure 4 (c–f) shows N_{hyd} and N_{SSIP} for the charged graphite systems. At the positively charged electrode (σ^+) the Li^+ keeps its almost perfectly tetra-hydrated solvation shell in both the 1 mol kg^{-1} and 10 mol kg^{-1} electrolytes, $N_{\text{hyd}} \approx 4$ at all z positions. Electrostatic repulsion keeps Li^+ out of the IHP, unlike in the σ^0 and σ^- systems. However, in the 20 mol kg^{-1} electrolyte, a small number of Li^+ ions penetrate the IHP, causing their hydration number to decrease to $N_{\text{hyd}} \approx 3$. The SSIP profile at σ^+ also matches that seen at σ^0 , but with a smaller interfacial decrease because fewer Li^+ ions are present near the surface.

Cl^- is somewhat insensitive to surface polarity. Its hydration number remains $N_{\text{hyd}} \approx 5-6$ across the entire double layer for 1 and 10 mol kg^{-1} , and decreases slightly to ≈ 4.8 at 20 mol kg^{-1} . SSIPs are virtually absent at 1 mol kg^{-1} , rise to ~ 3 per anion at 10 mol kg^{-1} , and

reach ~ 6 at 20 mol kg^{-1} . The N_{hyd} and N_{SSIP} profiles for Cl^- at the negative electrode begin slightly farther from the graphite, reflecting the marginal electrostatic repulsion. Consistent with the bulk-normalised density profiles, the liquid layering observed at the neutral interface persists upon charging, and the virtually identical ion-coordination motifs at neutral and polarised electrodes indicate that $\text{Li}^+ \text{-} \text{Cl}^-$ co-adsorption is an intrinsic feature of these systems.

The counterintuitive features of Li^+ adsorption at charged electrodes can be rationalised by considering both the ionic intermolecular bonding environments and the z -resolved charge density, $\rho_q(z)$, composed of water and ion contributions.⁶² As shown in Figure 5, the total charge density, $\rho_q^{\text{tot}}(z)$, closely follows the water contribution, $\rho_q^{\text{H}_2\text{O}}(z)$ in all systems, with minor deviations near the OHP. Thus, the interfacial electric field is governed by the spatial and orientational structure of water.

Naturally, the interface suppresses large local charge heterogeneities, constraining how number densities change upon charging. The equilibrium adsorption structure is the free-energy minimum that balances direct graphene-ion/graphene-water interactions with stabilisation from hydration, ion pairing, and water-water interactions, all while suppressing local charge accumulation encoded in $\rho_q^{\text{tot}}(z)$.

Because $\rho_q^{\text{tot}}(z)$ is set primarily by the water structure, the positions of the adsorption layers are largely fixed by solvation and packing. Charging the electrode primarily changes the occupancy of ion adsorption sites, not their location. Across all concentrations and electrode polarities, the first ion adsorption peaks are located in a region of net positive total charge, $\rho_q^{\text{tot}}(z) > 0$. In this framework, Dočkal and co-workers defined an ion as compatible when adsorption at its peak position reduces $|\rho_q^{\text{tot}}(z)|$, and incompatible when it increases it.^{62,63} Accordingly, Cl^- is compatible and its adsorption is electrostatically favourable, as it reduces the local positive charge, whereas Li^+ is incompatible and electrostatically unfavourable, since it increases it. Additionally, the intermolecular bonds between water and Cl^- are much weaker than those with Li^+ , allowing graphite's electric charge to influence Cl^- more strongly

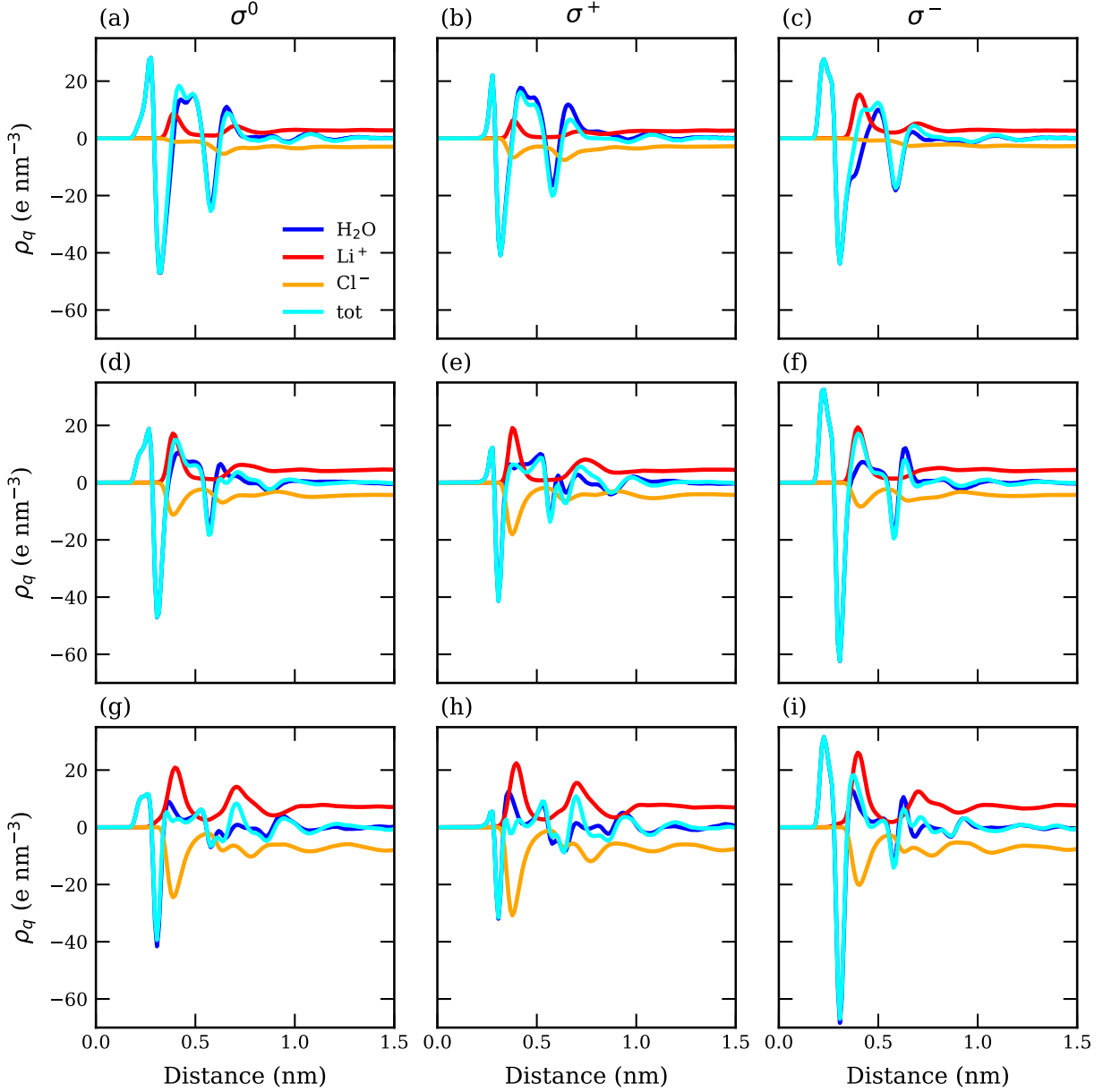


Figure 5: Charge density profiles, ρ_q^α (units $e \text{ nm}^{-3}$), for species $\alpha \in \{\text{H}_2\text{O}, \text{Li}^+, \text{Cl}^-\}$ and the total ($\alpha = \text{tot}$), as a function of z distance from the electrode. Columns correspond to electrode surface charge densities $\sigma^0 = 0 \text{ C m}^{-2}$ (left), $\sigma^+ = +0.0571 \text{ C m}^{-2}$ (middle), and $\sigma^- = -0.0571 \text{ C m}^{-2}$ (right). Rows show concentrations: (a–c) 1 mol kg^{-1} LiCl; (d–f) 10 mol kg^{-1} ; (g–i) 20 mol kg^{-1} . Colours: water (blue), Li^+ (red), Cl^- (yellow), total (cyan).

than Li^+ .

The observed trends follow from this picture. At 1 mol kg^{-1} (Figure 2 (a–c); Figure 5 (a–c)), positive charging markedly increases compatible Cl^- in the first adsorption layer, while incompatible Li^+ changes negligibly. The total charge density in the OHP-dominated by $\rho_q^{\text{H}_2\text{O}}(z)$ —also changes little, so there is no additional local electrostatic penalty for Li^+ beyond its direct repulsion from the electrode. Cl^- adsorption at the neutral surface is already negligible, so upon negative charging, neutralisation is achieved mainly by water reorientation and enhanced Li^+ adsorption. At 10 mol kg^{-1} (Figure 2 (d–f); Figure 5 (d–f)), both ions are abundant in the OHP of the neutral surface. Upon positive charging, water reorients so that $\rho_q^{\text{H}_2\text{O}}(z)$ —and consequently $\rho_q^{\text{tot}}(z)$ —in the OHP becomes less positive than at neutrality. This lowers the local electrostatic penalty and, counterintuitively, increases Li^+ accumulation in the OHP. In parallel, Cl^- adsorption in the OHP increases and SSIPs become more prevalent. Under negative charging, Cl^- adsorption decreases and Li^+ rises only marginally, reflecting the fact that $\rho_q^{\text{H}_2\text{O}}(z)$ in the OHP remains positive and comparable in magnitude to the neutral case, so the electrostatic driving force changes little. In the WiS 20 mol kg^{-1} system (Figure 2 (g–i); Figure 5 (g–i)), charging again modulates Cl^- more strongly than Li^+ . Positive charging decreases $\rho_q^{\text{H}_2\text{O}}(z)$ in the OHP and yields a slight increase of Li^+ together with a stronger increase of Cl^- . Unlike at 10 mol kg^{-1} , the negative electrode produces a more intuitive increase of Li^+ , consistent with the smaller amplitude of $\rho_q^{\text{H}_2\text{O}}(z)$ in the OHP, which reduces the role of compatibility.

Capacitance

The thickness of the EDL and its structure have a direct effect on the capacitance value (C_S), which can be calculated as the sum of the EDL (C_{EDL}) and quantum (C_Q) capacitance,

$$\frac{1}{C_S} = \frac{1}{C_Q} + \frac{1}{C_{\text{EDL}}}. \quad (9)$$

Both terms were extracted from QMMD simulations. The (integral) double-layer capacitance, C_{EDL} , which quantifies charge accumulation in the EDL, is obtained from

$$C_{\text{EDL}} = \frac{\sigma}{\Delta\Delta\Phi}, \quad (10)$$

where σ is the surface charge density and $\Delta\Delta\Phi = \Delta\Phi - \Delta\Phi^0$ is the change in the interfacial electrostatic potential drop upon charging. The value of $\Delta\Phi$ is computed as $\Delta\Phi = \Phi^{\text{electrode}} - \Phi^{\text{bulk}}$, where $\Phi^{\text{electrode}}$ is the electrostatic potential at the electrode surface and Φ^{bulk} is its value in the liquid bulk. The reference value $\Delta\Phi^0$ corresponds to $\Delta\Phi$ for a neutral electrode, otherwise known as the PZC. The potential profile $\Phi(z)$ is calculated from the planar-averaged charge density of all liquid species $\rho_q(z)$ by integrating Poisson's equation in one dimension,

$$\Phi(z) = -\frac{1}{\varepsilon_0} \int_0^z dz' (z - z') \rho_q(z'). \quad (11)$$

The differential quantum capacitance is obtained from the electronic density of states, $D(E)$, via

$$C_{\text{Q}}^{\text{diff}}(\Phi) = \frac{e^2}{4k_{\text{B}}T} \int_{-\infty}^{\infty} D(E) \operatorname{sech}^2 \left[\frac{E + \Phi}{2k_{\text{B}}T} \right] dE, \quad (12)$$

where E is measured relative to the Fermi energy, E_F , e is the elementary charge, k_{B} the Boltzmann constant, T the temperature, and Φ the electrostatic potential of the electrode. $D(E)$ was calculated as a trajectory average from each SCC-DFTB iteration using a Γ -centred Monkhorst-Pack $8 \times 8 \times 1$ k-point grid. The integral (charge-averaged) quantum capacitance that enters the series formula can be estimated as

$$C_{\text{Q}} = \frac{1}{\Delta\Phi} \int_0^{\Delta\Phi} C_{\text{Q}}^{\text{diff}}(\Phi) d\Phi. \quad (13)$$

Plots of $\Delta\Phi^0$, $\Delta\Phi^+$, and $\Delta\Phi^-$ are shown in Figure 6 for the negative ((a)) and positive ((b)) electrodes, together with the corresponding experimental $\Delta\Phi^0$ values, obtained from the minima of fourth-order polynomial fits to the measured differential capacitance curves against

Ag/AgCl (3.5 M KCl). C_{EDL} , C_Q and C_S for the negative and positive systems are presented in Figures 6 (c) and (d), respectively. The PZC, $\Delta\Phi^0$, increases up to 6 mol kg^{-1} as the Li^+ peak in the OHP grows while the small Cl^- peak remains nearly unchanged, thereby increasing the net positive charge stored in the double layer. Beyond 6 mol kg^{-1} , however, accumulation of Cl^- in the OHP offsets the positive charge from adsorbed Li^+ , leading to a decrease in $\Delta\Phi^0$ (Figure 6 (a, b)). Experimentally, the PZC decreases gradually between 5 and 19 mol kg^{-1} , with a total change of -0.11 V . This behaviour is qualitatively consistent with the simulations, which exhibit a decrease of -0.18 V between 6 and 20 mol kg^{-1} . Finney *et al.* likewise reported a concentration-dependent decrease in the PZC for aqueous NaCl at graphite, corroborated by simulation and experiment, indicating that this behaviour may also be applicable to other alkali halide salts at graphitic interfaces. Their work further showed that the EDL thickness follows a non-monotonic trend, decreasing before increasing beyond a threshold concentration due to oscillatory screening.^{28,29} At the negatively charged electrode, $\Delta\Phi^-$ remains nearly constant across all concentrations. As a result, the relationship between the excess drop $\Delta\Delta\Phi^-$ and concentration is dominated by the trend of $\Delta\Phi^0$, decreasing slightly up to 4 mol kg^{-1} , increasing between 4 and 10 mol kg^{-1} , and then plateauing at higher concentrations. C_{EDL} follows a similar trend, while C_Q increases between $1 - 2 \text{ mol kg}^{-1}$, then shows a steady decrease. Consequently, the total surface capacitance C_S stays nearly constant across the full concentration range (Figure 6). For the positive electrode, $\Delta\Phi^+$ is constant up to 4 mol kg^{-1} , falls between 4 and 10 mol kg^{-1} , and then plateaus. In combination with the shifting $\Delta\Phi^0$, this makes $\Delta\Delta\Phi^+$ fall from $1 - 6 \text{ mol kg}^{-1}$ and rise thereafter; C_{EDL} shows the inverse behaviour to $\Delta\Delta\Phi^+$, while C_Q is essentially constant between $1 - 4 \text{ mol kg}^{-1}$, decreases between $4 - 10 \text{ mol kg}^{-1}$ and then plateaus at higher concentrations. Again, the resulting C_S remains essentially independent of concentration (Figure 6 (d)).

Notably, as additional graphene layers are added, the quantum capacitance C_Q increases significantly.^{64,65} Therefore, the C_{EDL} contribution in the series relation (Equation 9) becomes more dominant. In the absence of an electronic bottleneck, C_S would simply track C_{EDL} , and

would increase in line with the structural changes to the EDL. Figures 6 (a–b) also reveal that the reference PZC, $\Delta\Phi^0$, varies appreciably with concentration and strongly influences the excess drop $\Delta\Delta\Phi$. For σ^- , $\Delta\Phi^-$ is almost concentration-independent, yet the decrease in $\Delta\Phi^0$ beyond 6 mol kg⁻¹ narrows $\Delta\Delta\Phi$ and yields the apparent rise in C_{EDL} . This dependence provides the mechanistic insight that changes at the neutral interface modify the excess potential required to reach a given σ and thus the integral capacitance. However, when capacitances from different electrolytes are compared, a common potential reference should be considered; otherwise, PZC shifts can be mistaken for genuine changes in performance.

Conclusions

In this work, molecular dynamics simulations combined with quantum-mechanical molecular dynamics have elucidated the intricate structural and electrochemical behaviour of concentrated and water-in-salt (WiS) aqueous LiCl solutions at graphitic electrodes. Across a broad concentration range (1 – 20 mol kg⁻¹), significant alterations in the electrical double layer (EDL) structure and ion distribution were observed, reflecting a complex interplay among ionic adsorption, hydration, and solvent-separated ion pair (SSIP) formation.

Bulk-normalised density profiles reveal pronounced changes in interfacial structure in concentrated and WiS LiCl solutions. At low concentrations (< 6 mol kg⁻¹), Li⁺ preferentially adsorbs at the electrode, resulting in a net positive charge within the outer Helmholtz plane (OHP) and an increase in the potential of zero charge (PZC). As the concentration rises beyond 6 mol kg⁻¹, the number density profiles show substantial Cl⁻ accumulation at the interface, driven by the formation of SSIPs and the limited availability of free water, yielding nearly overlapping Li⁺ and Cl⁻ density peaks in the WiS regime (16 – 20 mol kg⁻¹) and, with minimal contact ion-pairs.

These structural changes lead to an anomalous trend in EDL thickness as a function of electrolyte concentration. Unlike the classical Debye length prediction, which anticipates a

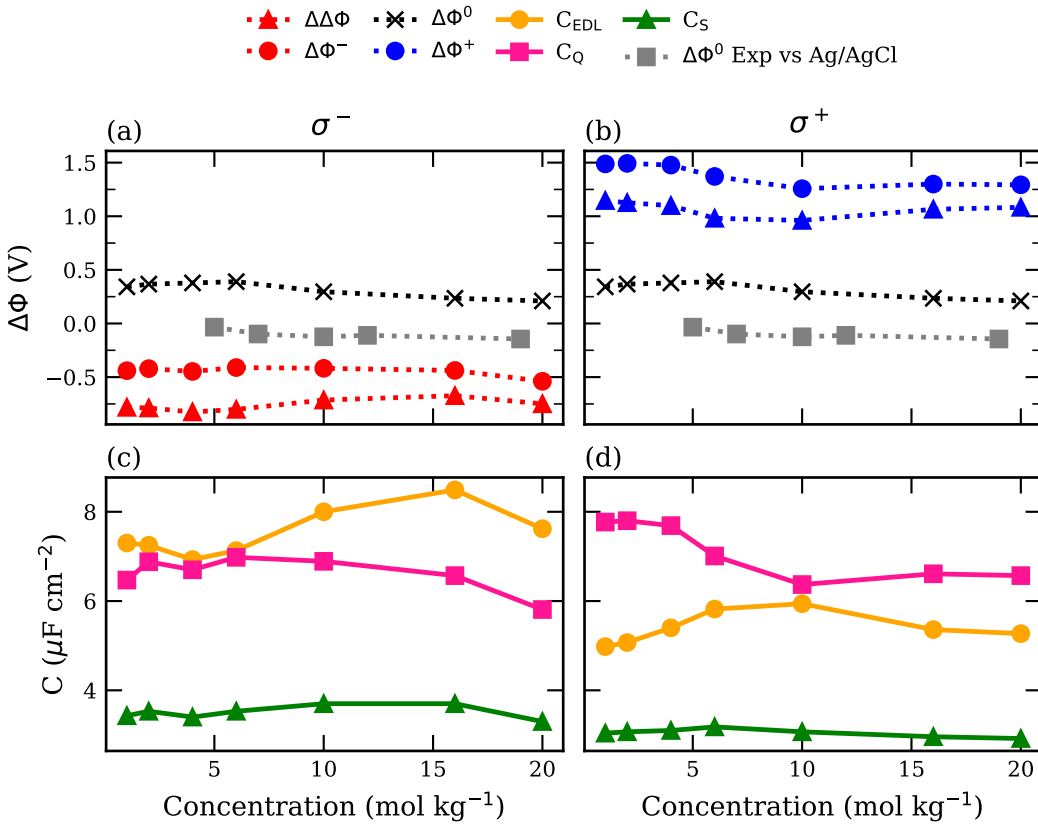


Figure 6: Concentration dependence of the interfacial potential drop and the surface-capacitance components of LiCl-graphite capacitor. (a) and (b) show the electrostatic potential difference $\Delta\Phi$ between the electrode plane and the bulk electrolyte for a negatively charged surface ($\sigma^- = -0.057 \text{ C m}^{-2}$, (a) and a positively charged surface ($\sigma^+ = +0.057 \text{ C m}^{-2}$, (b). Black crosses: $\Delta\Phi^0$ at the potential of zero charge (PZC); coloured circles: $\Delta\Phi^\pm$ at the charged electrodes; coloured triangles: the excess drop $\Delta\Delta\Phi = \Delta\Phi^\pm - \Delta\Phi^0$; grey squares: $\Delta\Phi^0$ measured from experimental differential capacitance vs an Ag/AgCl reference. (c) and (d) give the integral capacitances: the surface capacitance C_S (green), the integral double-layer capacitance C_{EDL} (pink), and the quantum capacitance C_Q (orange) for σ^- (c) and σ^+ (d). Dotted lines are guides to the eye. Error bars correspond to one standard error from block-averaging but are smaller than the symbol size and have therefore been omitted for clarity.

monotonic decrease with increasing ion concentration, the EDL thickness exhibited a non-monotonic and electrode charge-dependent behaviour. At neutral electrodes, the thickness initially decreases but subsequently increases beyond 4 mol kg^{-1} , driven by a lack of available free water and enhanced SSIP formation, leading to ion co-adsorption. Positively charged electrodes exhibit a similar but earlier (lower concentration) transition due to Cl^- ion accumulation inside the OHP for concentration as low as 2 mol kg^{-1} , whereas negatively charged electrodes show a monotonic increase in thickness with concentration.

These interfacial structural changes directly impact the electrostatic potential drop at the electrode-electrolyte interface and the capacitance values. As the concentration increases, the overlap of Li^+ and Cl^- density profiles in the OHP leads to enhanced charge compensation at the interface, reducing the net potential drop $\Delta\Phi^0$ at the PZC. This is in qualitative agreement with experimental measurements. For negatively charged electrodes, the potential drop at the surface remains nearly constant across concentrations, while shifts in the PZC primarily influence the excess drop $\Delta\Delta\Phi$. At positively charged electrodes, both the surface potential drop and $\Delta\Delta\Phi$ show a clearer dependence on electrolyte concentration, reflecting the earlier onset of anion accumulation. Despite the pronounced concentration-dependent trends in both EDL and quantum capacitances, their opposing behaviours cause the total surface capacitance, C_s , to remain largely insensitive to electrolyte concentration. Despite this, as the quantum capacitance, C_Q , increases with the number of graphene layers, the total capacitance approaches the EDL capacitance, C_{EDL} , in multilayer systems. These findings emphasise the critical role of interfacial structure in governing the electrochemical response and highlight the need to specify reference potentials when comparing capacitances across different electrolyte concentrations.

Acknowledgements

The work was conducted with support from EPSRC Centre for Doctoral Training “Graphene NOWNANO” (grant EP/L01548X/1). R.A.W.D. would like to thank the EPSRC for further support (grants EP/T01816X/1 and EP/V049925/1). Simulations were performed on the Computational Shared Facility at the University of Manchester.

Bibliography

- (1) Shin, S.-J.; Kim, D. H.; Bae, G.; Ringe, S.; Choi, H.; Lim, H.-K.; Choi, C. H.; Kim, H. On the importance of the electric double layer structure in aqueous electrocatalysis. *Nature communications* **2022**, *13*, 174.
- (2) Fedorov, M. V.; Kornyshev, A. A. Ionic Liquids at Electrified Interfaces. *Chemical Reviews* **2014**, *114*, 2978–3036.
- (3) Simon, P.; Gogotsi, Y. Perspectives for electrochemical capacitors and related devices. *Nature materials* **2020**, *19*, 1151–1163.
- (4) Rehl, B.; Ma, E.; Parshotam, S.; DeWalt-Kerian, E. L.; Liu, T.; Geiger, F. M.; Gibbs, J. M. Water structure in the electrical double layer and the contributions to the total interfacial potential at different surface charge densities. *Journal of the American Chemical Society* **2022**, *144*, 16338–16349.
- (5) Wu, Q.; Xu, Z. J. Mechanistic Insights into Cation Effects in Electrolytes for Electrocatalysis. *Angewandte Chemie International Edition* **2025**, *64*, e202505022.
- (6) Stern, O. Zur theorie der elektrolytischen doppelschicht. *Zeitschrift für Elektrochemie und angewandte physikalische Chemie* **1924**, *30*, 508–516.
- (7) Elliott, J. D.; Chiricotto, M.; Troisi, A.; Carbone, P. Do specific ion effects influence the physical chemistry of aqueous graphene-based supercapacitors? Perspectives from multiscale QMMD simulations. *Carbon* **2023**, *207*, 292–304.
- (8) Howard, J. J.; Perkyns, J. S.; Pettitt, B. M. The Behavior of Ions near a Charged Wall Dependence on Ion Size, Concentration, and Surface Charge. *The Journal of Physical Chemistry B* **2010**, *114*, 6074–6083.
- (9) Fedorov, M. V.; Kornyshev, A. A. Ionic liquid near a charged wall: Structure and

- capacitance of electrical double layer. *The Journal of Physical Chemistry B* **2008**, *112*, 11868–11872.
- (10) Laanait, N.; Mihaylov, M.; Hou, B.; Yu, H.; Vanýsek, P.; Meron, M.; Lin, B.; Benjamin, I.; Schlossman, M. L. Tuning ion correlations at an electrified soft interface. *Proceedings of the National Academy of Sciences* **2012**, *109*, 20326–20331.
- (11) Wang, J.; Bard, A. J. Direct atomic force microscopic determination of surface charge at the gold/electrolyte interface the inadequacy of classical GCS theory in describing the double-layer charge distribution. *The Journal of Physical Chemistry B* **2001**, *105*, 5217–5222.
- (12) Zhan, C.; Cerón, M. R.; Hawks, S. A.; Otani, M.; Wood, B. C.; Pham, T. A.; Stadermann, M.; Campbell, P. G. Specific ion effects at graphitic interfaces. *Nature communications* **2019**, *10*, 4858.
- (13) Hunger, J.; Schaefer, J.; Ober, P.; Seki, T.; Wang, Y.; Prädel, L.; Nagata, Y.; Bonn, M.; Bonthuis, D. J.; Backus, E. H. G. Nature of cations critically affects water at the negatively charged silica interface. *Journal of the American Chemical Society* **2022**, *144*, 19726–19738.
- (14) Borukhov, I.; Andelman, D.; Orland, H. Steric effects in electrolytes: A modified Poisson-Boltzmann equation. *Physical review letters* **1997**, *79*, 435.
- (15) Uematsu, Y.; Netz, R. R.; Bonthuis, D. J. The effects of ion adsorption on the potential of zero charge and the differential capacitance of charged aqueous interfaces. *Journal of Physics: Condensed Matter* **2018**, *30*, 064002.
- (16) Markiewitz, D. M.; Goodwin, Z. A.; Zheng, Q.; McEldrew, M.; Espinosa-Marzal, R. M.; Bazant, M. Z. Ionic Associations and Hydration in the Electrical Double Layer of Water-in-Salt Electrolytes. *ACS Applied Materials & Interfaces* **2025**, *17*, 29515–29534.

- (17) Elliott, J. D.; Papaderakis, A. A.; Dryfe, R. A.; Carbone, P. The electrochemical double layer at the graphene/aqueous electrolyte interface: what we can learn from simulations, experiments, and theory. *Journal of Materials Chemistry C* **2022**, *10*, 15225–15262.
- (18) Williams, C. D.; Dix, J.; Troisi, A.; Carbone, P. Effective Polarization in Pairwise Potentials at the Graphene–Electrolyte Interface. *The Journal of Physical Chemistry Letters* **2017**, *8*, 703–708.
- (19) Goloviznina, K.; Fleischhaker, J.; Binninger, T.; Rotenberg, B.; Ers, H.; Ivanistsev, V.; Meissner, R.; Serva, A.; Salanne, M. Accounting for the quantum capacitance of graphite in constant potential molecular dynamics simulations. *Advanced materials* **2024**, *36*, 2405230.
- (20) Jeanmairet, G.; Rotenberg, B.; Salanne, M. Microscopic simulations of electrochemical double-layer capacitors. *Chemical reviews* **2022**, *122*, 10860–10898.
- (21) McEldrew, M.; Goodwin, Z. A.; Kornyshev, A. A.; Bazant, M. Z. Theory of the double layer in water-in-salt electrolytes. *The journal of physical chemistry letters* **2018**, *9*, 5840–5846.
- (22) Becker, M.; Loche, P.; Rezaei, M.; Wolde-Kidan, A.; Uematsu, Y.; Netz, R. R.; Bonthuis, D. J. Multiscale Modeling of Aqueous Electric Double Layers. *Chemical Reviews* **2024**, *124*, 1–26.
- (23) Li, C.-Y.; Chen, M.; Liu, S.; Lu, X.; Meng, J.; Yan, J.; Abruña, H. D.; Feng, G.; Lian, T. Unconventional interfacial water structure of highly concentrated aqueous electrolytes at negative electrode polarizations. *Nature Communications* **2022**, *13*, 5330.
- (24) Di Pasquale, N.; Finney, A. R.; Elliott, J. D.; Carbone, P.; Salvalaglio, M. Constant chemical potential–quantum mechanical–molecular dynamics simulations of the graphene–electrolyte double layer. *The Journal of Chemical Physics* **2023**, *158*.

- (25) Vatamanu, J.; Borodin, O.; Olguin, M.; Yushin, G.; Bedrov, D. Charge storage at the nanoscale: understanding the trends from the molecular scale perspective. *Journal of Materials Chemistry A* **2017**, *5*, 21049–21076.
- (26) Wei, Z.; Elliott, J. D.; Papaderakis, A. A.; Dryfe, R. A.; Carbone, P. Relation between Double Layer Structure, Capacitance, and Surface Tension in Electrowetting of Graphene and Aqueous Electrolytes. *Journal of the American Chemical Society* **2024**, *146*, 760–772.
- (27) Dočkal, J.; Lísal, M.; Moučka, F. Molecular dynamics of the interfacial solution structure of alkali-halide electrolytes at graphene electrodes. *Journal of Molecular Liquids* **2022**, *353*, 118776.
- (28) Finney, A. R.; McPherson, I. J.; Unwin, P. R.; Salvalaglio, M. Electrochemistry, ion adsorption and dynamics in the double layer: a study of NaCl (aq) on graphite. *Chemical science* **2021**, *12*, 11166–11180.
- (29) Finney, A. R.; Salvalaglio, M. Properties of aqueous electrolyte solutions at carbon electrodes: effects of concentration and surface charge on solution structure, ion clustering and thermodynamics in the electric double layer. *Faraday Discussions* **2024**, *249*, 334–362.
- (30) Suo, L.; Borodin, O.; Gao, T.; Olguin, M.; Ho, J.; Fan, X.; Luo, C.; Wang, C.; Xu, K. "Water-in-salt" electrolyte enables high-voltage aqueous lithium-ion chemistries. *Science* **2015**, *350*, 938–943.
- (31) Borodin, O.; Self, J.; Persson, K. A.; Wang, C.; Xu, K. Uncharted waters: super-concentrated electrolytes. *Joule* **2020**, *4*, 69–100.
- (32) Vazquez, D. G.; Ingenmey, J.; Trapp, K. A.; Ciliak, D.; Salanne, M.; Lukatskaya, M. R. Extended Stability Window in Water-in-Salt Electrolytes: Understanding the Origins. *Journal of the American Chemical Society* **2025**, *147*, 35953–35961.

- (33) Attard, P. Asymptotic analysis of primitive model electrolytes and the electrical double layer. *Physical Review E* **1993**, *48*, 3604.
- (34) Adar, R. M.; Safran, S. A.; Diamant, H.; Andelman, D. Screening length for finite-size ions in concentrated electrolytes. *Physical Review E* **2019**, *100*, 042615.
- (35) Zeman, J.; Kondrat, S.; Holm, C. Bulk ionic screening lengths from extremely large-scale molecular dynamics simulations. *Chemical Communications* **2020**, *56*, 15635–15638.
- (36) Zeman, J.; Kondrat, S.; Holm, C. Ionic screening in bulk and under confinement. *The Journal of Chemical Physics* **2021**, *155*, 204501.
- (37) Lee, A. A.; Perez-Martinez, C. S.; Smith, A. M.; Perkin, S. Scaling analysis of the screening length in concentrated electrolytes. *Physical review letters* **2017**, *119*, 026002.
- (38) Le Breton, G.; Joly, L. Molecular modeling of aqueous electrolytes at interfaces: Effects of long-range dispersion forces and of ionic charge rescaling. *The Journal of Chemical Physics* **2020**, *152*, 241102.
- (39) Zeron, I. M.; Abascal, J. L. F.; Vega, C. A force field of Li+, Na+, K+, Mg2+, Ca2+, Cl-, and SO42- in aqueous solution based on the TIP4P/2005 water model and scaled charges for the ions. *The Journal of Chemical Physics* **2019**, *151*, 134504.
- (40) Abascal, J. L. F.; Vega, C. A general purpose model for the condensed phases of water: TIP4P/2005. *The Journal of Chemical Physics* **2005**, *123*, 234505.
- (41) Cornell, W. D.; Cieplak, P.; Bayly, C. I.; Gould, I. R.; Merz, K. M.; Ferguson, D. M.; Spellmeyer, D. C.; Fox, T.; Caldwell, J. W.; Kollman, P. A. A Second Generation Force Field for the Simulation of Proteins, Nucleic Acids, and Organic Molecules. *Journal of the American Chemical Society* **1995**, *117*, 5179–5197.
- (42) Werder, T.; Walther, J. H.; Jaffe, R. L.; Halicioglu, T.; Koumoutsakos, P. On the

Water-Carbon Interaction for Use in Molecular Dynamics Simulations of Graphite and Carbon Nanotubes. *The Journal of Physical Chemistry B* **2003**, *107*, 1345–1352.

- (43) Smith, L.; Wei, Z.; Williams, C. D.; Chircotto, M.; Pereira da Fonte, C.; Carbone, P. Relationship between Capillary Wettability, Mass, and Momentum Transfer in Nanoconfined Water: The Case of Water in Nanoslits of Graphite and Hexagonal Boron Nitride. *ACS Applied Materials & Interfaces* **2024**, *16*, 56316–56324.
- (44) Berendsen, H.; van der Spoel, D.; van Drunen, R. GROMACS: A message-passing parallel molecular dynamics implementation. *Computer Physics Communications* **1995**, *91*, 43–56.
- (45) Van Der Spoel, D.; Lindahl, E.; Hess, B.; Groenhof, G.; Mark, A. E.; Berendsen, H. J. C. GROMACS: Fast, flexible, and free. *Journal of Computational Chemistry* **2005**, *26*, 1701–1718.
- (46) Wood, H. O.; Burnett, H. M.; Dryfe, R. A. W.; Carbone, P. Stability and structure of the aqueous LiTFSI–LiCl interface. *Faraday Discuss.* **2024**, *253*, 212–232.
- (47) Elliott, J. D.; Troisi, A.; Carbone, P. A QM/MD Coupling Method to Model the Ion-Induced Polarization of Graphene. *Journal of Chemical Theory and Computation* **2020**, *16*, 5253–5263.
- (48) Hourahine, B.; Aradi, B.; Blum, V.; Bonafe, F.; Buccheri, A.; Camacho, C.; Cevallos, C.; Deshaye, M.; Dumitrică, T.; Dominguez, A.; others DFTB+, a software package for efficient approximate density functional theory based atomistic simulations. *The Journal of chemical physics* **2020**, *152*.
- (49) Elstner, M.; Porezag, D.; Jungnickel, G.; Elsner, J.; Haugk, M.; Frauenheim, T.; Suhai, S.; Seifert, G. Self-consistent-charge density-functional tight-binding method for simulations of complex materials properties. *Physical Review B* **1998**, *58*, 7260.

- (50) Orazem, M. E.; Pébère, N.; Tribollet, B. Enhanced graphical representation of electrochemical impedance data. *Journal of The Electrochemical Society* **2006**, *153*, B129.
- (51) Dočkal, J.; Moučka, F.; Lísal, M. Molecular dynamics of graphene–electrolyte interface: Interfacial solution structure and molecular diffusion. *The Journal of Physical Chemistry C* **2019**, *123*, 26379–26396.
- (52) Pascal, T. A.; Goddard, W. A. I. Entropic Stabilization of Water at Graphitic Interfaces. *The Journal of Physical Chemistry Letters* **2021**, *12*, 9162–9168.
- (53) Kirchner, K.; Kirchner, T.; Ivanistsev, V.; Fedorov, M. Electrical double layer in ionic liquids: Structural transitions from multilayer to monolayer structure at the interface. *Electrochimica Acta* **2013**, *110*.
- (54) Vatamanu, J.; Borodin, O.; Smith, G. D. Molecular dynamics simulations of atomically flat and nanoporous electrodes with a molten salt electrolyte. *Phys. Chem. Chem. Phys.* **2010**, *12*, 170–182.
- (55) Bohinc, K.; Kralj-Iglič, V.; Iglič, A. Thickness of electrical double layer. Effect of ion size. *Electrochimica Acta* **2001**, *46*, 3033–3040.
- (56) Bazant, M. Z.; Storey, B. D.; Kornyshev, A. A. Double Layer in Ionic Liquids: Over-screening versus Crowding. *Phys. Rev. Lett.* **2011**, *106*, 046102.
- (57) Guerrero-García, G. I.; González-Tovar, E.; Chávez-Páez, M.; Kłos, J.; Lamperski, S. Quantifying the thickness of the electrical double layer neutralizing a planar electrode: the capacitive compactness. *Physical Chemistry Chemical Physics* **2018**, *20*, 262–275.
- (58) Jäger, H.; Schlaich, A.; Yang, J.; Lian, C.; Kondrat, S.; Holm, C. A screening of results on the decay length in concentrated electrolytes. *Faraday Discussions* **2023**, *246*, 520–539.

- (59) Dočkal, J.; Svoboda, M.; Lísal, M.; Moučka, F. A general hydrogen bonding definition based on three-dimensional spatial distribution functions and its extension to quantitative structural analysis of solutions and general intermolecular bonds. *Journal of Molecular Liquids* **2019**, *281*, 225–235.
- (60) Dočkal, J.; Mimrova, P.; Lísal, M.; Moučka, F. Structure of aqueous alkali metal halide electrolyte solutions from molecular simulations of phase-transferable polarizable models. *Journal of Molecular Liquids* **2024**, *394*, 123797.
- (61) Ovalle, V. J.; Hsu, Y.-S.; Agrawal, N.; Janik, M. J.; Waegele, M. M. Correlating hydration free energy and specific adsorption of alkali metal cations during CO₂ electroreduction on Au. *Nature Catalysis* **2022**, *5*, 624–632.
- (62) Dočkal, J.; Lísal, M.; Moučka, F. Molecular dynamics of preferential adsorption in mixed alkali–halide electrolytes at graphene electrodes. *The Journal of Chemical Physics* **2022**, *157*, 084704.
- (63) Dočkal, J.; Rezlerová, E.; Předota, M.; Lísal, M.; Moučka, F. Understanding interfacial structure and preferential adsorption in mixed alkali-halide electrolytes at graphene oxide electrodes by constant potential molecular dynamics simulations. *Journal of Molecular Liquids* **2025**, *424*, 127078.
- (64) Zhan, C.; Neal, J.; Wu, J.; Jiang, D.-e. Quantum effects on the capacitance of graphene-based electrodes. *The Journal of Physical Chemistry C* **2015**, *119*, 22297–22303.
- (65) Yin, X.-T.; You, E.-M.; Zhou, R.-Y.; Zhu, L.-H.; Wang, W.-W.; Li, K.-X.; Wu, D.-Y.; Gu, Y.; Li, J.-F.; Mao, B.-W.; others Unraveling the energy storage mechanism in graphene-based nonaqueous electrochemical capacitors by gap-enhanced Raman spectroscopy. *Nature Communications* **2024**, *15*, 5624.